INSIGHTS ON ARTERIAL SECONDARY FLOW STRUCTURES AND VORTEX DYNAMICS GAINED USING THE MRV TECHNIQUE

Kartik V. Bulusu and Michael W. Plesniak
Department of Mechanical and Aerospace Engineering
The George Washington University
800 22nd Street, N.W., Washington, DC 20052
email: plesniak@gwu.edu

ABSTRACT

The purpose of this study is to gain an understanding of the formation of arterial secondary flow structures due to physiological parameters such as geometry (curvature), pulsatility and harmonics of inflow conditions. Accordingly, *in vitro* experimental investigation of arterial secondary flow structures was performed using the magnetic resonance velocimetry (MRV) technique at Stanford University. In this paper, we discuss the kinematics of vorticity in two regions of a 180^0 curved artery model viz., the entrance- (or straight-inlet pipe) and the 180° curved pipe-region. We applied the Womersley solution in the entrance-region to ascertain the unsteady pressure drop per unit length and in-plane vorticity for a pulsatile, carotid artery-based flow rate waveform. In the 180° curved pipe region a simple circulation budget was performed to discern vortex-splitting of large-scale Dean-type vortices.

INTRODUCTION

Arterial secondary flow structures are known to influence wall shear stress and exposure time of blood-borne particles that are closely related to atherogenesis, especially in arterial curvatures. Our research program is motivated by the clinical implications of spiral blood flow patterns associated with patient-specific diagnosis and pathology, wherein hemodynamics and coherent motions of vortices could potentially impact the overall cardiovascular health.

The experimental study presented in this paper is characterized by Equation 1 that relates the dimensionless pressure gradient in the streamwise direction (p_ℓ) in a tube with uniform curvature. In Equation 1, G is a superimposed mean pressure gradient in the otherwise (zero-mean) oscillatory pressure gradient, V is a dimensionless velocity amplitude and α is the Womersley number (Pedley, 1980).

$$-p_\ell = G + \alpha^2 \, V \, cos \, \alpha^2 t \qquad (1)$$

Waters & Pedley (1999) and Lyne (1971) among several others have analyzed problems of the type, $G = 0$ in Equation 1. One important outcome of their work is the characterization of a two-vortex system in the inviscid core that has been referred as the Lyne vortex system in the literature. The Lyne-system is considered to be inviscid and surrounded by a viscous Stokes layer. The Dean vortices generated within Stokes layer drive a two-vortex (Lyne) system in the opposite orientation.

This study deals with arterial flows where in general, $G \neq 0$ in Equation in 1. The central objective of this study is to develop an understanding the kinematics of vorticity in arterial secondary flow structures building on the MRV measurements made by Plesniak & Bulusu (2016).

Bulusu & Plesniak (2013) and Bulusu & Plesniak (2015) have discussed the spatio-temporal, evolution of the large-scale vortical structures associated with secondary flows, i.e. deformed Dean-, Lyne- and Wall-type (D-L-W) vortices. We hypothesize that the persistence of arterial secondary flow vortices as observed in two-dimensional cross-sections are intrinsically related to the influence of the out-of-plane flow and tilting that could be observed in three-dimensional fields. In addition, the unsteady pressure drop upstream to the curvature informed by the the degree of pulsatility in the flow provides that necessary boundary conditions in the flow field.

In this paper we present our analysis considering the following two regions of the 180^0 curved artery model: (i) Entrance region where the degree of flow pulsatility is described by the Womersley number and is defined as the ratio of transient inertia forces ($\rho \omega u$) and viscous forces ($\mu u / r^2$), albiet in straight pipes with oscillatory pressure gradient (Womersley, 1955) and (ii) The curved region where vortex decay-related phenomena such as spliting can be addressed via the viscous, material rate of change of circulation.

EXPERIMENTAL ARRANGEMENT

The MRV experiments on the curved artery model were performed at the Richard M. Lucas Center at Stanford University using a 3 Tesla General Electric (Model: Discovery 750 MRI system) whole body scanner with an eight-channel cardiac coil. We followed the guidelines of phase contrast MRI (PC-MRI) elegantly presented along with description of data acquisition and post-processing of three-component, three-dimensional (3C-3D) MRV measurements (Elkins & Alley, 2007; Pelc *et al.*, 1994). The curved artery model has pipe radius, $r = 0.25$ inches (or 0.00635 meters), inlet and outlet pipe lengths were approximately, 2 meters long and the curvature ratio, $\delta = r/R = 1/7$. Recent papers by Banko *et al.* (2015) and Jalal *et al.* (2016) outlines the benefit of MRV in comparison to other non-invasive techniques of velocity data acquisition and uncertainty in measurements.

Three-component, phase-averaged velocity data were obtained throughout the model volume at a spatial resolution of 0.6 mm in each Cartesian direction ($\approx 5\%$ of the diameter of the tube that is 12.7 mm). The scanned volume includes both the fluid and solid model walls. Wall identification was performed via thresholding based on the signal magnitude: voxels with magnitude greater than a preset-threshold value of the magnitude of the average noise were identified as fluid (Banko *et al.*, 2015). The evaluation of signal-to-noise ratios, measurement uncertainty due to velocity encoding and the partial volume effects can be ascertained following detailed discussions in Elkins & Alley (2007), Banko *et al.* (2015) and Pelc *et al.* (1994). Details

1

Table 1. MRV recording parameters

Flow geometry	3D - 180-degree curved artery test section
Imaging volume	200 mm × 116 mm × 21.6 mm
Imaging matrix	322 × 192 × 36
Temporal resolution	40 phases in 4 seconds
Spatial resolution	0.6 mm (isotropic)
Velocity encoding	R/L 80 cm/s
	A/P 40 cm/s
	S/I 90 cm/s

Table 2. Experimental hydrodynamic parameters

Curvature ratio	$\delta = \frac{r}{R}$	
Mean volumetric flow rate	Q_s	13.7 mL/s
Maximum volumetric flow rate	Q_{max}	61.1 mL/s
Amplitude ratio	$\gamma = \frac{Q_{max}}{Q_s}$	4.4
Waveform period	T	4 seconds
Mean Strouhal number	$St_{mean} = \frac{\omega r}{U_s}$	0.09
Mean Dean number	$K_{mean} = \frac{\sqrt{2}\,(U_s)\,r}{\nu}(r/R)^{\frac{1}{2}}$	102
Max. Dean number	$K_{max} = \frac{\sqrt{2}\,(U_{max})\,r}{\nu}(r/R)^{\frac{1}{2}}$	441 ($t/T = 0.175$)
Mean Reynolds number	$Re_{mean} = \frac{U_s\,d}{\nu}$	380
Max. Reynolds number	$Re_{max} = \frac{U_{max}\,d}{\nu}$	1650 ($t/T = 0.175$)
Womersley number	$\alpha = r(\omega/\nu)^{\frac{1}{2}} = (St_{mean}\,Re_{mean}/2)^{\frac{1}{2}}$	4.22

of our experiments and uncertainty in measurements can be found in Plesniak & Bulusu (2016). A programmable gear pump (Ismatec model BVP-Z) was used to provide the inflow (flow rate) and controlled using a MATLAB program with the NI-6229 data acquisition module. The phase-locked measurements in the MRI system were triggered by a pulse provided by the NI-6229 data acquisition module at onset of every cycle of the digitized carotid artery-based flow rate waveform as shown in Figure 1.

Velocity data were obtained in separate scans of 20 phase bins per period of the cardiac flow rate waveform. A total of 40 phase bins were reconstructed using linear interpolation in time. Data were acquired in 6 scans with the 'flow-on' and 4 scans with the 'flow-off'. The average 'flow-off' case was subtracted from each of the 'flow-on' phases to reduce the background noise and phase-errors in the velocity data during the post-processing. A total scan time for a single scan was $\approx$ 44 minutes, which is much longer than all flow time scales, with the run of 10 scans lasting $\approx$ 7 hours was performed. Post-processing of MRV data was performed using EnSight (v10.1.6) desktop data visualization software. A summary of the MRV recording parameters is presented in Table 1.

Blood-analog fluid and the physiological inflow waveform

The MRV experiments utilized Glycerol-DI water solution (40%/60% by weight) as the working fluid with the addition of a trace amount of copper sulfate to maximize signal intensity. The fluid kinematic viscosity was measured at 3.761($\pm$0.23) CSt (or 3.761×10^{-6} m^2/s) using a standard Ubbelhode viscometer at room temperature and and density, $\rho = 1078$ kg/m^3. The physiological carotid artery waveform was reconstructed from ultrasonic flowmeter measurements on the left carotid artery reported by Holdsworth et al. (1999). This waveform was discretized to 40 evenly-spaced instants (in time) spanning a period (T) of 4 seconds. The time interval between discretized points was 100 ms. All the experiments were performed at the controlled room temperature of $24^oC(\pm1^o)$.

A summary of the hydrodynamic experimental parameters is presented in Table 2. The values of Womersley number ($\alpha = 4.22$), mean Reynolds number (Re_{mean}) and one mean Dean number (K_{mean}) are reported for one complete cycle of the composite carotid artery flow rate waveform ($T = 4$ s) and a tube inner diameter of 12.7 mm (Figure 2A). The physiological waveform is the superposition of multiple harmonic frqeuncies and therefore, each harmonic can be associated with a unique Womersley (α), mean Reynolds

(Re_{mean}) and a mean Dean number (K_{mean}) as discussed in greater detail in the analysis presented in this paper.

RESULTS AND DISCUSSION

The analysis for vorticity estmation and circulation of large-scale vortices presented in this paper was broken into two regions viz., entrance region and curved region. The entrance region does not have large-scale vortices but has vorticity predominantly in the near-wall region. Additionally, the circulation in the large-scale vortices in the curved artery model changes due to the viscous forces acting on it. These abstractions can be viewed from the point of view of vortex lines that are tangent to the vorticity vectors as discussed in the results and analyses that follow.

Estimation of vorticity in the entrance region

The pulsatile flow rate [$Q(t)$] was measured at the location upstream of the curved pipe. The upstream flow conditions can be decomposed into a steady and the oscillatory flow parts, i.e. the ensuing pressure, velocity and flow rate can be written as a linear combination of steady and oscillatory parts of the flow i.e., $p(z,t) = p_s + \hat{p}(z,t); u(z,t) = u_s + \hat{u}(z,t); Q(t) = Q_s + \hat{Q}(t)$.

Consequently, the governing equation can be grouped into the steady and the oscillatory parts for corresponding Poiseuille flow and Womersley flow solutions:

$$\frac{\partial p_s}{\partial z} - \mu\left(\frac{\partial^2 u_s}{\partial r^2} + \frac{1}{r}\frac{\partial u_s}{\partial r}\right) = 0 \qquad (2)$$

$$\rho\frac{\partial \hat{u}}{\partial t} + \frac{\partial \hat{p}}{\partial z} - \mu\left(\frac{\partial^2 \hat{u}}{\partial r^2} + \frac{1}{r}\frac{\partial \hat{u}}{\partial r}\right) = 0 \qquad (3)$$

From MRV measurements we calculated the pulsatile flow rate [$Q(t) = \int_S (u_z(r)|_t \cdot \hat{n})dS$]. The corresponding steady pressure ($\frac{dp_s}{dz}$) and oscillatory pressure drops per unit length ($\frac{d\hat{p}(t)}{dz}$) needed to be calculated for vorticity esti-

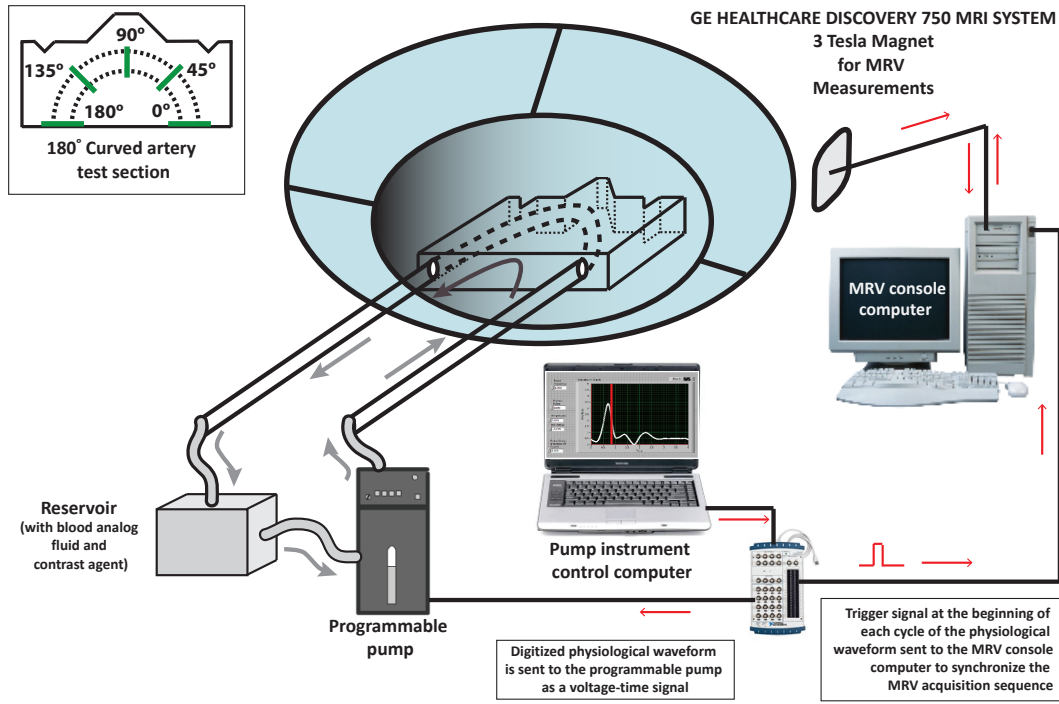Figure 1.   Experimental set-up 180° curved tube model for curved arteries

mates. The solution of the steady (Poiseuille) flow problem (Equation 2) is $Q_s = \frac{p_1 - p_2}{8\mu\ell}\pi r^4$, where the pressure drop per unit length is $\frac{dp_s}{dz} = \frac{p_1 - p_2}{\ell}$.

The following oscillatory flow solution of Equation 3 was derived by Womersley (1955), for a pressure drop per unit length assumed to be a periodic function in time ($\frac{d\hat{p}(t)}{dz} = \frac{p_1 - p_2}{\ell} = Ae^{i\omega t}$):

$$\hat{Q}(t) = \frac{\pi r^2}{\rho}\frac{A}{i\omega}\{1 - \frac{2\alpha i^{3/2}}{i^3\alpha^2}\frac{J_1(\alpha i^{3/2})}{J_0(\alpha i^{3/2})}\}e^{i\omega t} \qquad (4)$$

In Equation 4 the angular frequency is $\omega = 2\pi f$ and the amplitude is A. Further, $\alpha = r\sqrt{\frac{\rho\omega}{\mu}}$, is known as the Womersley number and J_0, J_1 are Bessel functions of the first kind of order-zero and order-one, respectively.

The oscillatory part, $\hat{Q}(t)$), is a complicated periodic function. It is expressed it as a Fourier series (or sum of n-harmonics), the sum of n-cosines and n-sines and substituted it into the Womersley solution (Equation 4) to calculate the oscillatory pressure drop per unit length.

The oscillatory part of the flow rate, $\hat{Q}(t)$, is shown in Figure 2A, along with the certain harmonics ($n = 1, 3, 10$). In Figure 2B, a_n and b_n are the Fourier coefficients in the summation equation inset in the figure. There are few obvious attributes can be associated with Figures 2A and B. The 1st-harmonic clearly has the same time period as the time period (T) of the composite oscillatory waveform ($\hat{Q}(t)$) and consequently, the same frequency ($f_1 = 1/T = 1/4$ Hz). The successive harmonics (n=2,3,...) have frequencies that are scalar multiples of the 1st-harmonic frequency ($f_1 = 0.25$ Hz, $f_2 = 0.5$ Hz, $f_3 = 0.75$ Hz,...). This can be observed in the frequencies corresponding to a_n and b_n in Figure 2B. The partial sums of harmonics are shown in Figure 2C, to demonstrate that the sum of 10-harmonics was suf-

ficient to reconstruct the composite oscillatory waveform. This can also be ascertained from Figure 2B, wherein the magnitude of the Fourier coefficients from 11th-harmonic onward were negligible. The pressure drop per unit length, $\frac{d\hat{p}_n(t)}{dz}$, was calculated for each harmonic (n) of the composite oscillatory flow rate, $\hat{Q}_n(t)$, using Equation 4. The dimensionless pulsatile flow rate, $Q(t)/Q_s = (Q_s + \hat{Q}(t))/Q_s$, and the analytically-calculated dimensionless pressure drop per unit length, $\frac{dp(z,t)/dz}{dp_s/dz}$, plotted over one time period (T) in Figure 2D. It should be noted that a phase-lag between pressure gradient and flow rate waveforms are clearly noticed with the pressure gradient leading the flow rate.

The direction of vorticity vectors in the entrance region lie on the cross-sectional planes of the tube. Therefore, the in-plane vorticity-component is effectively in the $\theta - direction$ ($r - \theta - z$ coordinate system). In Figures 2E and F, we present the variation of the real part of dimensionless, upstream, in-plane vorticity ($\frac{\vec{\omega}_\theta}{2\pi f}$), with the radius ($r/r_{max}$) as the parameter, the frequency associated with the 1st-harmonic ($f = 0.25$ Hz and the time period, $T = 4$ s) of the composite flow rate waveform. The vorticity is also taken as the linear summation of the steady and oscillatory parts obtained after calculating the curl of the steady and oscillatory velocity vector fields. It should be noted in Figure 2E, that at certain radii, the vorticity vectors reverse their direction following the pulsatile velocity profiles and their corresponding pressure drops. The phase-lag of vorticity (Figure 2F) is ascertained from the driving pressure drop per unit length in the entrance region. The near-wall, $\vec{\omega}_\theta$-component (at $r/r_{max} = 1$) is proportional to the shear stress along the entrance region. Figure 2G is a schematic representation of the vortex lines under pulsatile inflow conditions ($\vec{u}_z(r,t)$) in entrance region of the curved artery model. A representation of these vortex lines can be seen in Figure 3 upstream of the 4°-location, wherein there is minimal out-of-plane vorticity.
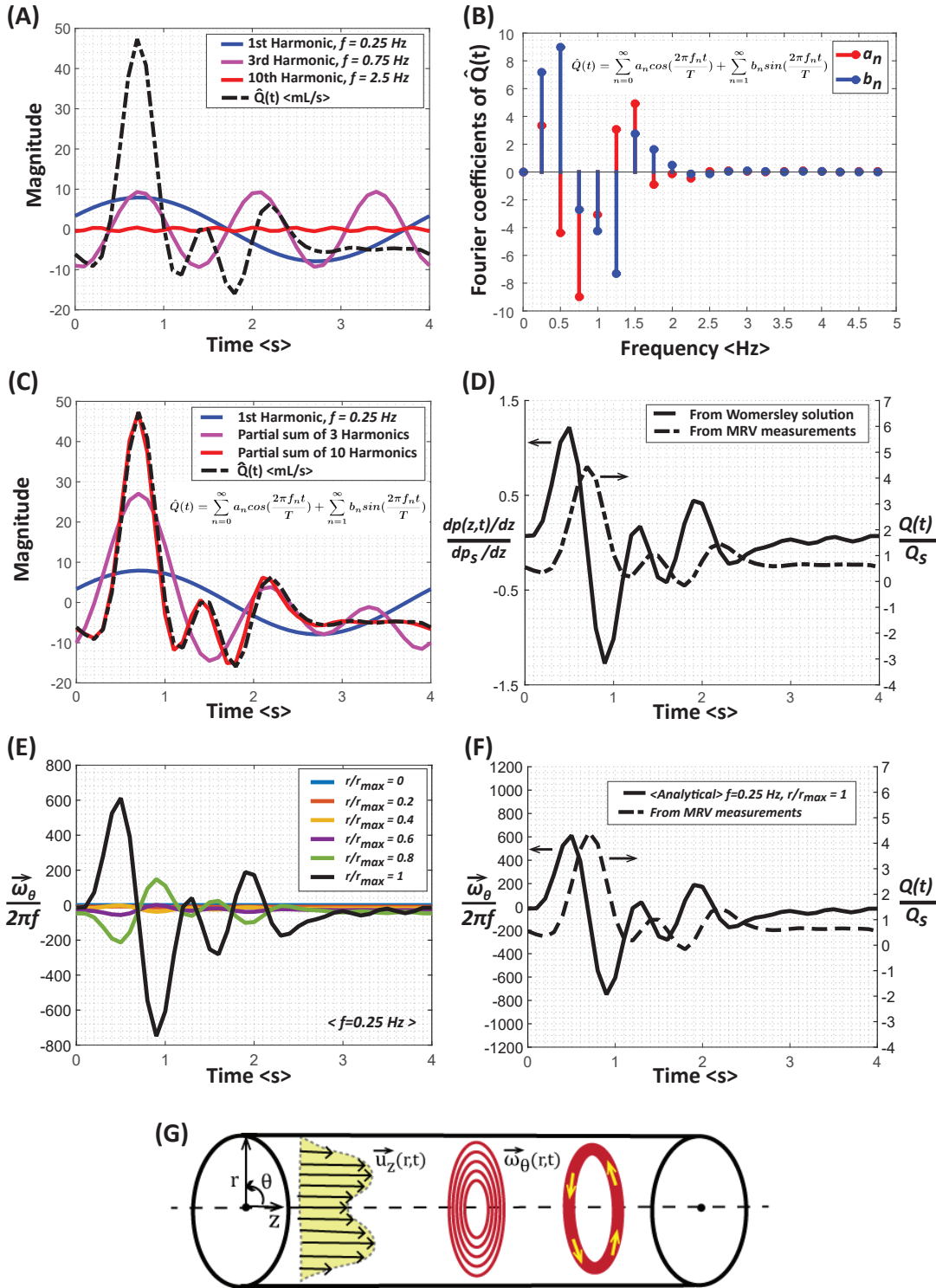
3

Figure 2. Entrance region flow conditions (A) Harmonics of oscillatory flow rate, $\hat{Q}(t)$ (B) Fourier coefficients of $\hat{Q}(t)$ (C) $\hat{Q}(t)$ as a partial sum of harmonics (D)MRV-based dimensionless flow rate and Womersley solution-based dimensionless pressure drop (E) Dimensionless vorticity ($\frac{\vec{\omega}_\theta}{2\pi f}$) at various pipe radii (F) Wall vorticity (G) Schematic representation of vortex lines in the entrance region

Material volume-based circulation budget analysis in the curved region

A precursor to the circulation budget analysis was the characterization of out-of-plane (secondary flow) vorticity in the native toroidal coordinate system using wavelet decomposition methods at various angular cross-sections in

the 180^0 curved artery model. Secondary flow structures are conceptually modeled as swirling vortical structures that are either rotation-dominated or strain-dominated. Cartesian velocity components (u_x, u_y, u_z) acquired during MRV sequence were transformed into special toroidal components (u_r, u_ψ, u_θ) using EnSight software (v10.1.6), , where θ is
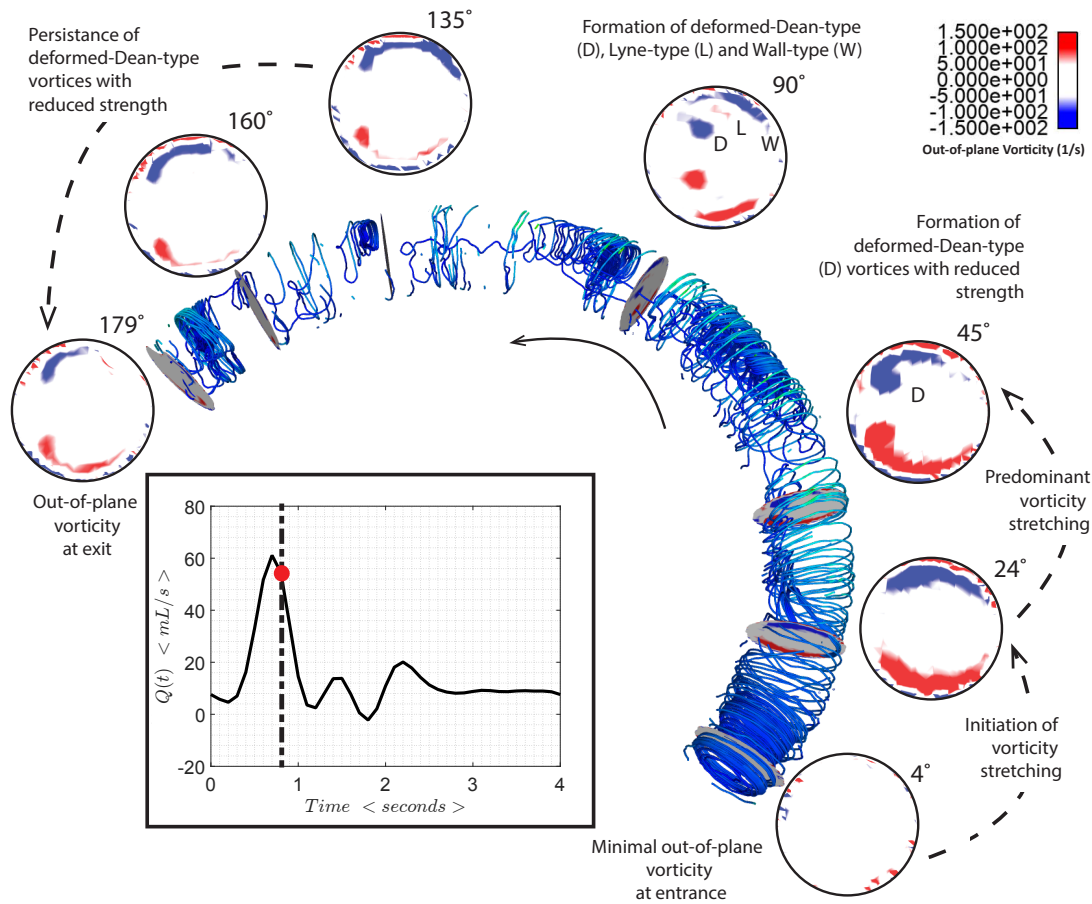
4

Figure 3. Three-dimensional representation of flow in the 180^0 curved artery model with out-of-plane vorticity marked at various locations indicating the large-scale (D-L-W) vortices. Inset: Physiological flow rate waveform shows the time-instance at which these data were acquired

the axial or out-of-plane direction. The transitional secondary flow structures were observed exclusively at various cross-sectional locations (Figure 3). We used our wavelet-decomposition algorithm (PIVlet 1.2) that performs wavelet transforms on vorticity data ($\tilde{\omega}$) and accurately resolved of the Dean-, Lyne- and Wall-type vortices with size-structure and strength considerations (Bulusu & Plesniak, 2013; Bulusu *et al.*, 2014; Bulusu & Plesniak, 2015; Plesniak & Bulusu, 2016).

We examined the rate of change of circulation within control regions encompassing the large-scale vortical structures associated with (D-L-W) secondary flow structures at planar cross-sections. Figure 3 shows the out-of-plane vorticity contours in various cross-sections and the paths traced by particles in the vorticity field and are representative of vortex lines. In fact, vortex lines cannot end within the flow field unlike a few lines in Figure 3. This abberation can be attributed to some complexities in computing and constrains in EnSight software (v10.1.6). However, these traces are in general parallel to the vorticity vector field and representative of vortex lines that undergo stretching and tilting up to the 45^0- location as shown in Figure 3. The formation of the D-type vortices, their persistence and decay are clearly shown in Figure 3. The Wall-type vortices (W) are known to "fork" from the D-type vortices between the 45°- and 90°-locations as discussed in a recent paper by Plesniak & Bulusu (2016). For circulation budget analysis we treated a collection of vortex lines as those seen in Figure 3 or mate-

rial curves around which circulation is computed. We used the material derivative of the viscous, rate of change of circulation in the streamwise (θ) direction, ($\frac{D\Gamma}{Dt} = \frac{D}{Dt} \oint_C \vec{u} \cdot d\vec{s}$) and expressed it in the following equation where ν is the kinematic viscosity of the blood-analog fluid:

$$\frac{D\Gamma}{Dt} = -\nu \iint_S (\vec{\nabla} \times \vec{\nabla} \times \vec{\omega}) \cdot \hat{n} dA \qquad (5)$$

In Equation 5 the left-hand-side, should equal the right-hand side for conservative external forces. However, we hypothesized that the equation may yield an inequality due to phenomena such as vortex splitting in complex, pulsatile arterial flows be subjected to complicated forcing. We restricted our analysis to the 45°-, 90° and 135°-planar, cross-sectional locations in the three-dimensional flow field assuming contiguity of the ensuing vortex tubes representing the large-scale, Dean-type vortices. In Figures 4B, C and D, we show this inequality clearly during the time-instances in the deceleration phase (marked in Figure 4A). We observed that the rate of change of circulation and the viscous dissipation do not balance during the late deceleration phase. For example, during the late deceleration phase at the 90°- and 135°-locations, there is change from D-type to D-W-type system following the schematic representation presented in Figure 4A and the red and blue lines are not coincidental.
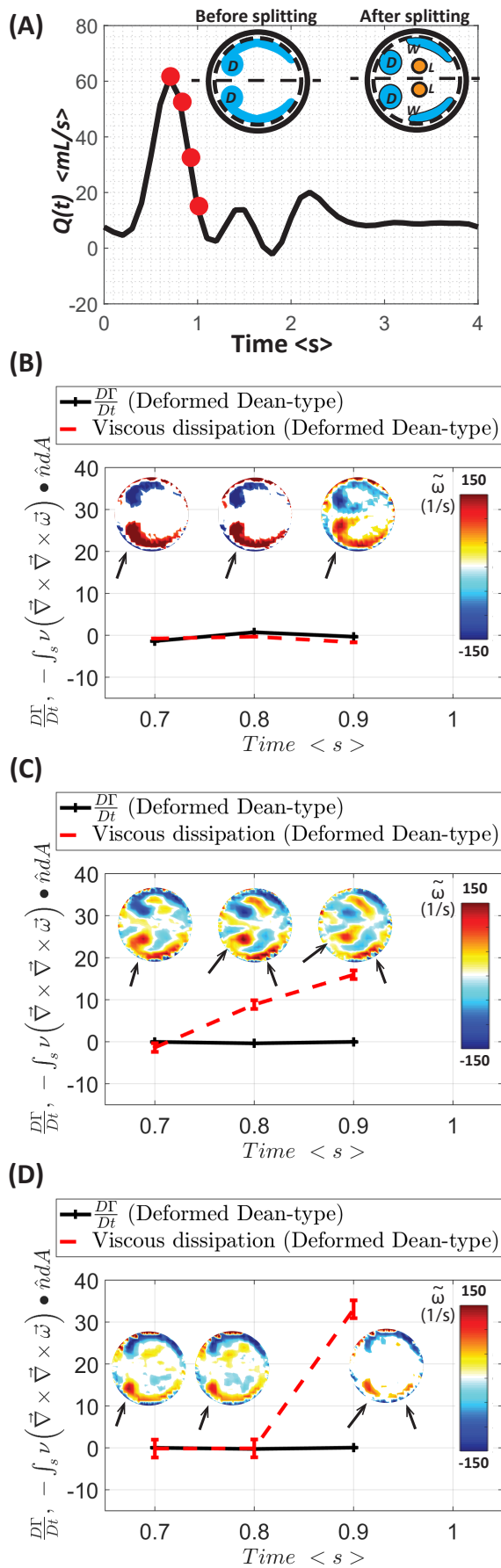
5

Figure 4. Viscous circulation budget with material volume consideration (A) Time-instances in the physiological waveform where the analysis was performed (Inset: Schematic representation of vortex splitting) (B) 45°-location (C) 90°-location (D) 135°-location

CONCLUSIONS

The 3C-3D MRV-experiments performed at Stanford University led to the visualization of the full 3D-velocity field in the curved artery model drawing on the benefit of tracer-particle-free approach. Informed by the MRV-based flow rate measurements the analytical pressure drop per unit unit length in the entrance region is deduced. In the classic Womersley solution the flow rate is determined for a known periodic pressure drop function, making our analysis the "inverse of the Womersley solution". The entrance region analysis showed that the in-plane vorticity vectors may change direction depending on the instantaneous pulsatile velocity profile. The circulation budget analysis in the 180° curved region is a potential indicator of vortex splitting since the presence of viscous disspative forces lead to the splitting and decay of large-scale arterial secondary flow structures.

REFERENCES

Banko, A., Coletti, F., Schiavazzi, D., Elkins, C. & Eaton, J. 2015 Three-dimensional inspiratory flow in the upper and central human airways. *Exp Fluids* **56**, 117–128.

Bulusu, K. V., Hussain, S. & Plesniak, M. W. 2014 Determination of secondary flow morphologies by wavelet analysis in a curved artery model with physiological inflow. *Exp Fluids* **55**, 1832.

Bulusu, K. V. & Plesniak, M. W. 2013 Secondary flow morphologies due to model stent-induced perturbations in a 180-degree curved tube during systolic deceleration. *Exp Fluids* **54** (3), 1493–1506.

Bulusu, K. V. & Plesniak, M. W. 2015 Shannon entropy-based wavelet transform method for autonomous coherent structure identification in fluid flow field data. *Entropy* **17** (10), 6617–6642.

Elkins, C. J. & Alley, M. T. 2007 Magnetic resonance velocimetry: applications of magnetic resonance imaging in the measurement of fluid motion. *Exp Fluids* **43**, 823–858.

Holdsworth, D.W., Norley, C. J., Frayne, R., Steinman, D. A. & Rutt, B. K. 1999 Characterization of common carotid artery blood-flow waveforms in normal human subjects. *Physiol. Meas.* **20(3)**, 219–240.

Jalal, S., Nemes, A., de Moortele, T. Van, Schmitter, S. & Coletti, F. 2016 Three-dimensional inspiratory flow in a double bifurcation airway model. *Exp Fluids* **57: 148**.

Lyne, W. H. 1971 Unsteady viscous flow in a curved pipe. *J. Fluid Mech.* **45**, 13–31.

Pedley, T. J. 1980 *The fluid mechanics of large blood vessels*. Cambridge University Press.

Pelc, N. J., Sommer, G., Li, K. C. P., Brosnan, T. J., Herfkens, R. J. & Enzmann, D. R. 1994 Quantitative magnetic resonance flow imaging. *Magn. Reson. Q.* **10** (3), 125–147.

Plesniak, M. W. & Bulusu, K. V. 2016 Morphology of secondary flows in a curved pipe with pulsatile inflow. *J. Fluids Eng* **138** (10), 101203.

Waters, S. L. & Pedley, T. J. 1999 Oscillatory flow in a tube of time-dependentcurvature. part 1. perturbation to flow in a stationary curved tube. *J. Fluid Mech.* **383**, 327–352.

Womersley, J. R. 1955 Method for the calculation of velocity, rate of flow and viscous drag in arteries when the pressure gradient is known. *J. Physiol.* **1**, 553–563.

6